# Ernst-Moritz-Arndt University of Greifswald

## Master Thesis

---

# Kinetic effects in RF discharges

---

*Author:*
Philipp Hacker

*Supervisor:*
Prof. Dr. Ralf Schneider

*A thesis submitted in fulfillment of the requirements
for the degree of Master of Science - Physics*

*in the research group of*

Computational Sciences,
Institute of Physics

August 27, 2017

# Acknowledgements

The acknowledgments and the people to thank go here, don't forget to include your project advisor. . .

"Without encroaching upon grounds appertaining to the theologian and the philosopher, the domain of natural sciences is surely broad enough to satisfy the wildest ambition of its devotees. [. . .] The work may be hard, and the discipline severe; but the interest never fails, and great is the privilege of achievement. "

— John William Strutt, 3rd Baron Rayleigh, 1884
*in: Address to the British Association in Montreal*

# Declaration of Authorship

I hereby certify that this thesis has been composed by me and is based on my own work, unless stated otherwise. No other person's work has been used without due acknowledgement in this thesis. All references and verbatim extracts have been quoted, and iall sources of information, including graphs and data sets, have been specifically acknowledged.

. . . . . . . . . . . . . . . . . . . . . . .
*Signature of author*
Greifswald; August 27, 2017

# Contents

# List of Abbreviations

| abbreviation | full expression |
|---|---|
| e.g. | exempli gratia; *for example* |
| etc. | et cetera; *and so on* |
| ac | alternating current |
| dc | direct current |
| rf, RF | radio frequency |
| ccrf | capacitively coupled radio frequency |
| EDF | energy distribution function |
| EDV | *german: Energieverteilungsfunktion*, energy distribution function |
| EEDF | electron energy distribution function |
| IEDF | ion energy distribution function |
| p., pp. | page, plural pages |
| ff. | folio; *on the (next) page*, ablative of folium (*page*) |
| SIE, SEE | secondary ion/electron emission |
| HWA | hard wall approximation |
| MS | mass spectrometer |
| PROES | phase resolved emission spectroscopy |
| MWI | microwave interferometer |
| AN | antenna |
| FC | flow controller |
| PIC | particle-in-cell |
| MCC | Monte-Carlo-Colissions |

x

| abbreviation | full expression |
| --- | --- |

**Table 1**: List of abbreviations and their corresponding phrases. If specified, the translation or an equivalent expression is written.

x

x

# Physical Quantities

| Quantity | Unit | Symbol | Dimension | Value |
|---|---|---|---|---|
| Speed of Light | m/s | $c_0$ | $L^1 T^{-1}$ | $2.997 \cdot 10^8$ |
| thermal velocity | m/s | $v_{\mathrm{th,j}}$ | $L^1 T^{-1}$ | |
| drift velocity | m/s | $v_{\mathrm{D,j}}$, $u_{\mathrm{j}}$ | $L^1 T^{-1}$ | |
| Boltzmann constant | eV/K | $k_{\mathrm{B}}$ | $M^1 L^2 T^{-2} K^{-1}$ | $8.617 \cdot 10^{-23}$ |
| mobility | cm$^2$/Vs | $\mu_{\mathrm{j}}$ | $I^1 T^2 M^{-1}$ | |
| planck constant | eVs | $\hbar$ | $G^{-1/2} c^{6/2} \varepsilon_0^{1/2}$ | $4.1345 \cdot 10^{-15}$ eVs $6.646 \cdot 10^{-34}$ Js |
| kinetic temperature | eV | $T_{\mathrm{j}}$ | $M^1 L^2 T^{-2}$ | $1\,\mathrm{eV} = 1.902 \cdot 10^{-19}$ K |
| elementary charge | C | $e$ | $I^1 T^1$ | $1.902 \cdot 10^{-19}$ |
| electric charge | C | $Q$, $q$ | $I^1 T^1$ | |
| particle mass | kg | $m_{\mathrm{j}}$ | $M^1$ | electron: $9.109 \cdot 10^{-31}$ ion: $5.310 \cdot 10^{-26}$ anion: $5.143 \cdot 10^{-26}$ |
| reduced mass | kg | $\mu_{\mathrm{j,k}}$ | $M^1$ | |
| distance,location | cm | $r$, $\vec{r}$ | $L^1$ | |
| Debye length | cm | $\lambda_{\mathrm{D,j}}$ | $L^1$ | |
| particle distance | cm | $\bar{b}$ | $L^1$ | |
| mean free path | cm | $s_{\mathrm{mfp,j}}$ | $L^1$ | |
| particle density | cm$^{-3}$ | $n_{\mathrm{j}}$ | $L^{-3}$ | |
| Vacuum permittivity | F/m | $\varepsilon_0$ | $M^{-1} L^{-3} T^{-4} A^2$ | $8.854 \cdot 10^{-12}$ |
| electrostatic potential | V | $\Phi$, $U$ | $M^1 L^2 I^{-1} T^{-3}$ | |
| electric current | As | $I$, $J$ | $I^1$ | |
| electric current density | As/cm$^2$ | $j_{\mathrm{j}}$ | $I^1 L^{-2}$ | |
| electric charge density | C/cm$^3$ | $\rho$ | $I^1 T^1 L^{-3}$ | |

| Quantity | Unit | Symbol | Dimension | Value |
|----------|------|--------|-----------|-------|
| electric resistance | $\Omega$ | $R$ | $M^1 L^2 T^{-3} I^{-2}$ | |
| electric capacity | F | $C$ | $M^{-1} L^{-2} T^4 I^2$ | |
| time | s | $t$ | $T^1$ | |
| plasma frequency | Hz | $\omega_{p,j}$ | $T^{-1}$ | |
| collisional frequency | Hz | $\nu_j$ | $T^{-1}$ | |

**Table 2**: Physical properties in their commonly — or for this purpose most convinient — units and corresponding SI units. If not specified, the values of each quantity refer to the afore-mentioned units.

# Abstract

The Thesis Abstract is written here and usually kept to just this page. The page is kept centered vertically so it can expand into the blank space above the title too.

# Chapter 1

# Physical Properties of Low Temperature RF Plasma

In this first chapter I will provide the necessary physical background for this work about the numerical simulation of low temperature capacitively coupled radio frequency plasma. Here both the mathematical basics and method for the simulation, as well as the most important aspects about the plasma properties will be explained.

## 1.1 Plasma Physics

### 1.1.1 Capacitively Coupled Radio Frequency Plasma

The experiment where after the conducted simulations is modelled after revolves around a capacitively coupled radio frequency, low temperature plasma at low pressures of oxygen. Here, I will refer to a plasma as an globally quasi-neutral gas, consisting of freely moving charges — e.g. electrons, positively and negatively ions — and neutral gas particles. The ratio between charged and neutral species defines the *degree of ionization*, which in this case is very low. The term of global neutrality emphasizes the purpose for different length scales inside the gas itself. Hence, the associated condition of neutrality by equal densities $n_e = n_i$ only is valid for areas larger than the so called *Debye sphere*. Inside this ball with a radius of $\lambda_D$ the *Debye length*, the afore-mentioned neutrality is not satisfied.

The creation of a plasma is accomplished by 2 parallel metal plates, the electrodes, where on at least one an ac signal at radio frequency is applied — this kind of experimental setup is among the most common, thus being used for basic but also in-depth studies of the afore-mentioned discharges. Here, a rf signal at exactly $13.56\,\mathrm{MHz}$ with an amplitude between $100$–$1000\,\mathrm{V}$ will be used. This equals to a wavelength of $22.11\,\mathrm{m}$ for the electric field wave, which is orders of magnitude higher than the eventually simulated experiment. The use of external magnetic fields is not within the scope of this work — correspondingly, the experiment I will refer to, also did not include any kinds of magnetic confinement or manipulation.

That said, a multitude of electric setups are possible, such as coated or grounded electrodes. Therefore, different regimes of operation ensue. For example, differently driven or shaped metal plates heavily influence the charge creation process inside the plasma. In summary,

the electrodes, neutral gas and electric layout resemble a dielectric hindered plate capacitor. This simplification can be used to access important physical properties, such as an additional voltage offset on one of the electrodes or charge currents at such. A basic scheme of an asymmetric rf discharge can be seen in figure 1.1. In the case of different electrode sizes, as seen in the scheme, the potential inside the spatially restricted area between wall and discharge can change drastically. This plasma sheath forms also between grounded parts of discharge containment or probes and plasma volume. This additional direct current offset is called *self-bias* (see section 1.1.4). A dielectric displacement current between plasma sheath and volume accommodates as a result of the different time scales of particle movement (see section 1.1.5).

Especially, self-bias and displacement current play a key role in the following investigations, as a capacitive coupling between electrodes and power supply is difficult to model in a numerical kinetic simulation. A strong mathematical analysis of general plasma properties would not be suitable for this kind of work, although certain aspects will be discussed later, such as in section 1.1.4 and section 1.1.5. In comparison to other low temperature, low pressure discharges — an example could be a dielectric hindered dc discharge at high voltages, with an electrode space gap of just a couple millimeters —, radio frequency plasma are characterized by their unique transport process inside the sheath and heating mechanisms of charged species. A more in-depth discussion can be found in section 1.1.6.
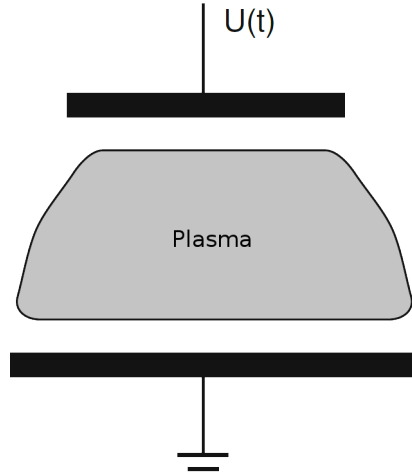


**Figure 1.1**: Schematic of an asymmetric discharge with one grounded and one driven electrode [13].

### 1.1.2   Plasma-Wall Interaction

In the discharges bulk, neutral gas particles are excited by electron collisions and radiating visible light. However, areas around, e.g. floating metal surfaces, probes and grounded walls are darker than the bulk. This is due to the low electron density and kinetic energy in this *plasma sheath*. Though areas with vanishing electron numbers can glow because of high collision efficiencies and/or frequencies.

Electrons, in general, are of a much higher mobility $\mu_\mathrm{e}$ and thermal velocity $v_\mathrm{th,e}$. Hence they impinge onto walls and surfaces more often than other species, leading to a — in this case we consider an electronegative oxygen discharge, where the following can be assumed true — negative charge and potential.

#### 1.1.2.1   Child-Langmuir Law

For an asymmetric ccrf discharge, dc *self bias* and displacement current are important parts of the electric system. Hence, the *Child-Langmuir Law* as a function of those properties can be written. The rf component of the excitation is neglected.

A greatly negative charged wall at $x = 0$ shall be a barrier for electrons of thermal velocity, e.g. $|\Phi(0) - \Phi(d)| \ll k_B T_e/e$. The thickness of the sheath shall be considered $d$. In an one-dimensional approach [13], the electron density $n_e(x)$ can be written with a *Boltzmann* distribution function $f_B(\Phi)$:

$$n_e(x) = n_e(d) \cdot f_B(\Phi) = n_e(d) \cdot \exp\left(\frac{e(\Phi(x) - \Phi(d))}{k_B T_e}\right) \quad . \tag{1.1}$$

This means that the electron density decreases exponentially towards the negatively charged wall. It can be assumed that the sheath thickness $d \ll s_{\mathrm{mfp,i}}$ the mean free path of the ions inside the plasma bulk. Hence, ions enter the sheath collisionless.

At the boundary between bulk and pre-sheath, the walls potential vanishes because of the plasmas shielding capabilities. Here, the ions are at $v_{i,0}$ speeds, therefore their density becomes:

$$n_i(x) = n_i(d)\left(1 - \frac{2e\Phi(x)}{m_i v_{i,0}^2}\right)^{-1/2} \tag{1.2}$$

Futhermore, one can assume that the kinetic energy at this point is smaller than the potential energy for the acceleration inside the pre-sheath, e.g. $m_i v_{i,0}^2 \ll |e\Phi(x)|$. Using *Poisson's* equation, and taking into account the ion-sheath interaction, equation 1.3 gives an equation for $\Phi(x)$:

$$\Delta\Phi \cong -\frac{en_i(-d)}{\varepsilon_0}\left(-\frac{2e\Phi(x)}{m_i v_{i,0}^2}\right)^{-\frac{1}{2}} \tag{1.3}$$

Solving this, and using the unpertubated ion current $j_i = n_i(d)ev_{i,0}$, one yields the result by *Langmuir*.

$$\Phi(x) = \left(\left(\frac{3}{4}(x+d)\right)^4 \left(\frac{j_i}{\varepsilon_0}\right)^2 \frac{m_i}{2e}\right)^{\frac{1}{3}} \tag{1.4}$$

Again, solving equation 1.4 for the current $j_i$ yields the *Child-Langmuir Law* (see equation 1.5). This equation defines the ion current as a function of the unperturbed plasma bulk. In other words, the sheath changes its thickness in dependency of those certain discharge parameters, always satisfying the ion current defined by the *Child-Langmuir Law*.

$$j_i = \frac{4}{9}\varepsilon_0\left(\frac{2e(\Phi(-d) - \Phi(0))^3}{m_i d^2}\right)^{\frac{1}{2}} \tag{1.5}$$

#### 1.1.2.2 Surface Effects and Secondary Ion Emission

Although plasma sheath physics are influenced by bulk properties, such as temperatures and densities, the space charge area itself is mainly characterized by processes of the wall. Hence an important aspect is the absorption and re-emission of ions and electrons. Those species than have unique features, like e.g. high velocities. Let's assume the associated metal wall behind the sheath ideally absorbs all impinging, charged particles, which recombine immediately near the surface.

**Secondary Electron Emission**   The discharges electrons are much faster and mobile than the other species, leading to the afore-mentioned negative charging and potential drop towards the wall. This accelerates the ion species up to *Bohm velocity* — see section 1.1.3 for a more in-depth discussion of the *Bohm criteria* and the ions sheath physics.

Continuity and charge conservation must be satisfied, hence the fluxes $J_\mathrm{j}$ of the species $j$ must be equal at the sheath edge — into and out of the sheath:

$$J_\mathrm{e} = J_\mathrm{i} \tag{1.6}$$

The mentioned potential drop $\Delta\Phi$ from section 1.1.2.1, beside accelerating positive ions, reflects negative charges slower than $v \leq \sqrt{2e\Delta\Phi/m}$. Similar to equation 1.1, the electron current towards the wall can be written. Here the first moment of the electron velocity $\langle v \rangle$ is used, calculated in equation 1.8 with the electron energy distribution function (EEDF) $f_\mathrm{e}(v)$:

$$j_\mathrm{e} = -\frac{e}{4}n_\mathrm{e}\langle v \rangle \exp\left(-\frac{e\Delta\Phi}{k_\mathrm{B}T_\mathrm{e}}\right) \tag{1.7}$$

$$\langle v \rangle = \int_\mathbb{R} v \cdot f_\mathrm{e}\left(v\right) \mathrm{d}v \tag{1.8}$$

Impinging ions are neutralized before impact by particles from the electron gas in the wall. Like before, any produced neutrals are reflected and exit the sheath collisionless — the mean free path is larger than the sheath thickness. Hence ionization is a process almost exclusively happening in the bulk or the pre-sheath.

Assuming a fast electron impacts on the wall, there is a chance of colliding with and liberating a second electron from the target. Here, the *secondary electron emission* coefficient is noted as $\gamma$: an impinging electron emits $\gamma$-many electrons from the metal. This *SEE* reduces the $\Delta\Phi$ because of an addition charge current from the wall towards the sheath edge, therefore altering the continuity condition $j_\mathrm{i} = j_\mathrm{e}$. A new *effective potential drop* $\Delta\Phi_\mathrm{eff}$ can be written in equation 1.9. According to [2] there is a critical value $\gamma_\mathrm{c}$ from which on the wall potential is unstable, leading to shifting sheath edges — the sheath edge oscillates with the rf signal anyway — and strong currents from the wall.

$$\Delta\Phi_\mathrm{eff} = -\frac{k_\mathrm{B}T_\mathrm{e}}{e} \cdot \ln\left((1-\gamma)\sqrt{\frac{m_\mathrm{i}}{2\pi m_\mathrm{e}}}\right) \tag{1.9}$$

**Secondary Ion Emission**   Research prior to this thesis [9] indicates that ions are produced near the surface of a metal electrode and heavily accelerated in the plasma sheath. In theory, secondary emission by surface ionization — in analogy to the surface neutralization — occurs with incident atoms of thermal energy. Hence one assumes a positively biased wall at high temperatures as the target. It's valence level is therefore broadened, giving an atom $A$ the chance the deposit an electron at the metal. After equilibrating thermally, a positive ion is emited by chance. This statistical process can be described by a thermodynamic equation (see equation 1.10) yielding the ionization coefficient of $A$. In equation 1.10 a modified approach for the *Saha-Langmuir equation* on the degree of ionization in gases can be found. Here, the surface's temperature $T$ and average work function $\overline{\Phi}_+$ are needed. Additionally, the ionization energy $I(A)$ — or impact energy —, the particle number currents of both species $j$ and $j^+$, corresponding statistical weights $w$, $w^+$ and reflection coefficients at the intrinsic potential

barrier $r/r^r$ are used.

$$A \leftrightharpoons A^+ + e^-$$

$$\alpha^+(A^+) = \frac{j^+}{j} = \frac{(1-r^+)\,w^+}{(1-r)\,w} \cdot \exp\left(\frac{\overline{\Phi}_+ + e\sqrt{eV_{\text{ext}}} - I(A)}{k_{\text{B}}T}\right) \tag{1.10}$$

At high temperatures of, e.g. $1000\,\text{K}$ and externally applied potentials $V_{\text{ext}} < 1\,\text{kV}$, the reflection associated *Schottky term* $e\sqrt{eV_{\text{ext}}}$ and the corresponding coefficients $r/r^+$ can be neglected — it appears to be just half of the thermal energy at room temperature. Though a theoretical approach is possible, there have not been accurate studies of such coefficients for temperatures around $300\,\text{K}$.

In addition to SIE of positive ions, a case for negative ions can be easily derived with small changes to equation 1.10: a negatively biased electrode is assumed and the average work function yields a different sign. The electron affinity of the incident particle $B$ is noted as $A(B)$.

$$B + e^- \leftrightharpoons B^-$$

$$\alpha^-(B^-) = \frac{(1-r^-)\,w^-}{(1-r)\,w} \cdot \exp\left(\frac{-\overline{\Phi}_- + e\sqrt{eV_{\text{ext}}} + A(B)}{k_{\text{B}}T}\right) \tag{1.11}$$

Applying the former assumptions to both equations of positive and negative ions, inserting a homogeneous work function $\Phi = \overline{\Phi}_- = \overline{\Phi}_+$ for the used substrate yields the originally derived *Saha-Langmuir equations*.

$$\alpha^+(A^+) = \frac{w^+}{w} \exp\left(\frac{\Phi - I(A)}{k_{\text{B}}T}\right), \qquad \alpha^-(B^-) = \frac{w^-}{w} \exp\left(\frac{-\Phi + A(B)}{k_{\text{B}}T}\right) \tag{1.12}$$

Though only considering atomic particle beams onto the wall until this point, forms similar to equation 1.12 can be derived for molecular surface interactions [8]. In case of the earlier discussed ccrf discharges, arguments like high temperatures can not be applied, hence the need for measured reflection coefficients.

Works of, e.g. [18] and [11] investigated ion beam scattering, electron loss and transport in plasma sheath environments for metal walls, especially MgO(100) surfaces. There Ustaze et al. studied incident oxygen gas particles — ions and neutrals — on magnesium oxyde surfaces. Impinging atoms became negatively charged ions, picking up electrons from the MgO of the wall. This interaction, though requiring a minimum ionization and liberation energy for the electron, is most effective at low energies $< 1\,\text{eV}$. This is due to a maximum of residence time at the target for an incoming atom. Hence it can be considered a non-resonant charge transfer process at the anion site. For an more in-depth discussion of both electron loss and capture for anion transport processes at walls one should consider [8].

Here, due to the lack of theoretical and experimental data on ion surface production, an ion beam onto the wall will result in a anion current in opposing direction of

$$j_- = \eta\, j_+ \ , \tag{1.13}$$

with a corresponding efficiency of an incident positive particle $\eta$. One should keep in mind the reaction of the plasma sheath and potential inside to an additional anion current from the wall. Also, the same stability criteria apply for $\eta$ as they do for the electron emission coefficient $\gamma$. In case of SIE beyond a critical value $\eta_{\text{c}}$, a second plasma sheath may develop, enclosing the bulk and an inner sheath and reducing transport in-between.

### 1.1.3   Bohm Criteria

In section 1.1.2 the behaviour of charge particle densities inside the plasma sheath has been discussed. In contrast to the discharge volume, those densities do not satisfy the quasi-neutrality condition in a distance of $d$ from the wall any more. Though we know that the sheath is a spatially restricted area around electrostatic floating surfaces, a physical law concerning this circumstance has not been derived here. So the question ensues, why the area of electron depletion does not extend further into the discharge volume.

To answer this question, one has to take a look at a substitutional system. This will be a, likewise mechanical, one-body extremal problem of a point mass. In this case only kinematic potentials with inverted parabolic maxima are of interest. Therefore, in this unstable equilibrium, a small pertubation culminates into a large force on the test body.

To see the quality of this example, one has to take a look at the second order differential equation of the afore-mentioned mechanical problem and the electrostatic *Poisson's equation* (see equation 1.14).

$$m\frac{\mathrm{d}^2\vec{r}}{\mathrm{d}t^2} = -\frac{\mathrm{d}V}{\mathrm{d}\vec{r}} \quad \Leftrightarrow \quad \Delta_{\vec{r}}\Phi = -\frac{\mathrm{d}\Psi}{\mathrm{d}\Phi} = f(\Phi) \overset{\text{Poisson's}}{=} \frac{\rho}{\varepsilon_0} \tag{1.14}$$

For an instability, the force on the test body must increase with the distance from the equilibrium, hence the equation 1.16 is used to calculate the exact velocity at which an ion is entering the sheath. This results in the first *Bohm criteria*.

$$0 > \left.\frac{\mathrm{d}^2\Psi}{\mathrm{d}\Phi^2}\right|_{\Phi=0} \overset{\text{equation 1.14}}{=} \left.\frac{\mathrm{d}}{\mathrm{d}\Phi}\left(\frac{n_\mathrm{e}(x) - n_\mathrm{i}(x)}{\varepsilon_0}\right)\right|_{\Phi=0} \frac{en_\mathrm{e}(-d)}{\varepsilon_0}\left(\frac{e}{k_\mathrm{b}T_\mathrm{e}} - \frac{e}{m_\mathrm{i}v_\mathrm{i,0}^2}\right) \tag{1.15}$$

$$\Rightarrow \quad v_\mathrm{i,0} \geq v_\mathrm{i,B} = \sqrt{\frac{k_\mathrm{B}T_\mathrm{e}}{m_\mathrm{i}}} \tag{1.16}$$

Analoguos you can define the so called *Mach number* $M = v_\mathrm{i,0}/v_\mathrm{i,B}$, where $v_\mathrm{i,B}$ denotes the *Bohm velocity*.

Now, to understand why the sheath does not extend further than a fixed distance $d$ from the discharge boundary, the particle movement has to be investigated on a smaller scale. As seen above, there is an electric field in the *pre-sheath* that accelerates the ions to $v_\mathrm{i,B}$. In addition,
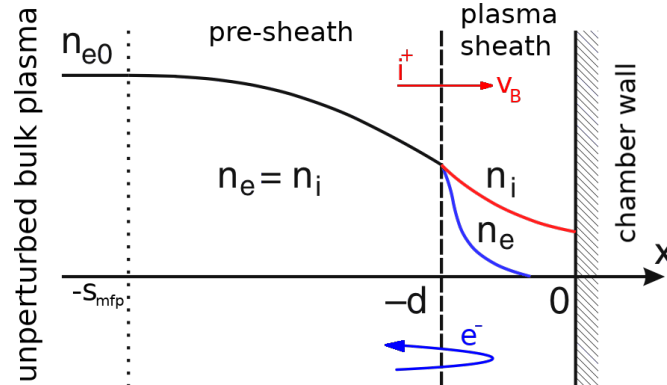


**Figure 1.2**: One dimensional density profiles as a function of the distance to a floating wall. Note the exponential decrease of the electron density $n_\mathrm{e}$ from the sheath border towards the presumably negatively charged wall. Densities allready reach approximately $0{,}66n_\mathrm{e,0}$ inside the pre-sheath. [13]

quasi-neutrality is still satisfied here:

$$n_\text{i}(x) = n_{\text{i},0} \exp\left(\frac{e\Phi(x)}{k_\text{B}T_\text{e}}\right) = n_\text{e}(x) \ . \tag{1.17}$$

Still, $\Phi(x)$ is the potential inside the pre-sheath from section 1.1.2 and $n_{\text{i},0}$ the unperturbed density from the plasma *bulk*. A greater part of the ion transport process in this area is governed by collisions with neutral gas particles, hence the velocity distribution function with the collision frequency $\nu_{\text{n,i}}$ has to be rewritten:

$$\frac{\text{d}v_\text{i}}{\text{d}x} = \frac{\nu_{\text{n,i}} v_\text{i}^2}{v_\text{B}^2 - v_\text{i}^2} \ \ . \tag{1.18}$$

From the singularity in equation 1.18 at $v_\text{i} = v_\text{B}$ and the knowledge of $\Phi(x)$ at the wall, one can calculate the sheath thickness $d$. Furthermore, ions with velocities smaller than the Bohm velocity are being accelerated inside the pre sheath. According to equation 1.16 velocities greater than $v_\text{B}$ are not allowed here. This is, together with equation 1.18 the reason why the ion velocity is exactly $v_\text{B}$ at the boundary of the plasma sheath and thus a positive space-charge ensues.

$$M \geq 1 \Leftrightarrow v_\text{i}(-d) \geq v_\text{B} \tag{1.19}$$

Conclusively, at the sheath boundary equation 1.19 is satisfied.
At $x = -d$, both negative and positive charge density decreased to $n_\text{i} = n_\text{e} \approx 0.66\,n_{\text{e},0}$ (see figure 1.2), where the potential is approximately $-k_\text{B}T_\text{e}/2e$ because of the currents onto the wall. In summarization, the plasma does not 'see' its sheath, because the ion dynamic discussed before is spatially restricted. The sheath only develops where there is electron depletion or an externally applied, negative potential.

### 1.1.4  Self Bias Voltage

An important step towards the electric characterization of such ccrf discharges is the development of a replacement circuit, see figure 1.4. Thus, one can define a specific impedance for a rf discharge of excitation frequency $\omega$. The value of $\varepsilon_\text{p}$ resembles the permeability of the working gas between the driven and/or grounded electrode [13]. In addition, this volume has the capacity $C_\text{p}$ — the capacity of a cubicle with a cross section $A$, thickness $b$ and electron-neutral collision frequency $\nu_{\text{e,n}}$ calculates like equation 1.20.

$$\varepsilon_\text{p} = 1 - \frac{\omega_{\text{p,e}}^2}{\omega(\omega - \mathbf{i}\nu_{\text{e,n}})} , \qquad C_\text{p} = \varepsilon_\text{p} C_0 = \varepsilon_\text{p} \varepsilon_0 \frac{A}{b} \tag{1.20}$$

$$Z_\text{p} = \left(\mathbf{i}\omega C_\text{p} + \frac{1}{\frac{1}{\omega_{\text{p,e}}^2 C_0}(\nu_{\text{e,n}} + \mathbf{i}\omega)}\right)^{-1} \tag{1.21}$$

The equation 1.21 represents the full electrical impedance, consisting of the inverse sum of real and imaginary resistance, as well as the capacity of the neutral gas volume. Here, $\mathbf{i}\omega/(\omega_{\text{p,e}}^2 C_0)$ characterizes the electrons inertia in regard to an external excitation $\omega$. The real part $\nu_{\text{e,n}}/(\omega_{\text{p,e}}^2 C_0)$ denotes the resistance by neutral particle collisions.

For high excitation frequencies, e.g. 13.56 MHz the bulk impedance can be neglected (see equation 1.21, [7]). Both sheath capacities of anode and cathode take the dominant part. Therefore, the discharge potential and voltage can be written as:

$$U(t) = U_{\mathrm{sb}} + U_{\mathrm{rf}} \sin(\omega t) ,$$
$$\Phi_{\mathrm{p}}(t) = \overline{\Phi_{\mathrm{p}}} + \Phi_{\mathrm{rf}} \sin(\omega t) \qquad (1.22)$$

Both electrodes sheath collapses completely during a full cycle of $U_{\mathrm{rf}}(t)$, which is why charges can impinge onto the surface and force the plasma potential $\Phi_{\mathrm{P}}$ to equal out locally with the walls. A short circuit between plasma and sheath occurs when $\Phi_{\mathrm{P}}$ becomes negative with regard to the excitation. The equation 1.23 and figure 1.3 express this circumstance.

$$\Phi_{\mathrm{p}}\max = \overline{\Phi_{\mathrm{p}}} + \Phi_{\mathrm{rf}} \geq U_{\mathrm{sb}} + U_{\mathrm{rf}} ,$$
$$\Phi_{\mathrm{p}}\min = \overline{\Phi_{\mathrm{p}}} - \Phi_{\mathrm{rf}} \geq 0 . \qquad (1.23)$$
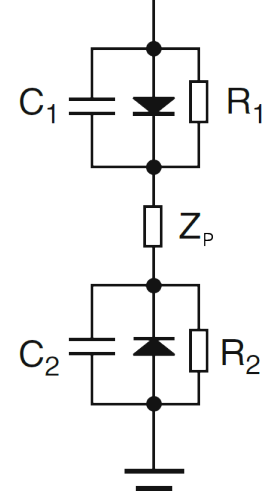
**Figure 1.4**: Replacement circuit of an asymmetrically driven ccrf discharge. [13] A diode represents the directed electron current from the sheaths $j = 1,2$.
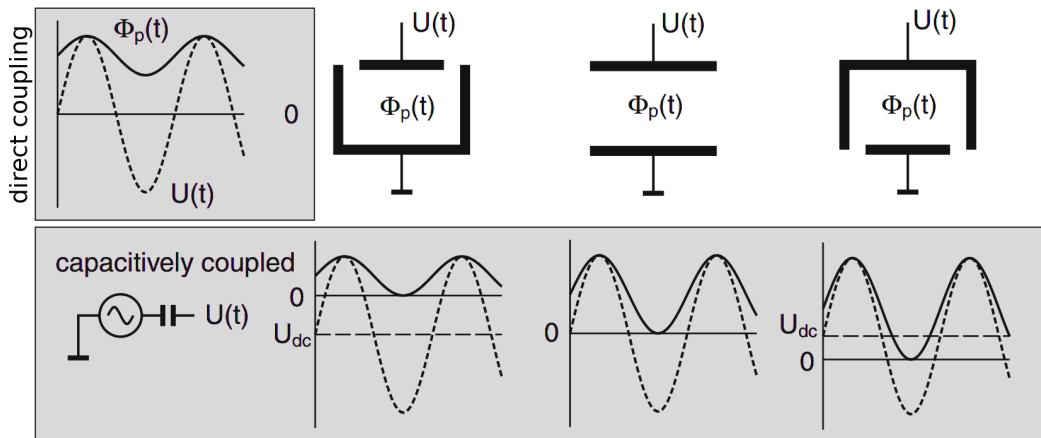
If there is no special coupling between electrode and electrical driver, the equality in equation 1.23 is true. However, if a capacitive coupling is used, there can't be any net current between excitation and electrode. The capacitance can not be inverted over the course of one rf cycle. The electron currents are then equal on both electrodes, therefore shifting the minimum plasma potential to ground and the maximum to the excitation. Finally, the dc *self bias* part $U_{\mathrm{sb}}$ and the mean plasma potential $\overline{\Phi_{\mathrm{p}}}$ are

$$\overline{\Phi_{\mathrm{p}}} = \frac{1}{2}(U_{\mathrm{sb}} + U_{\mathrm{rf}}) , \qquad U_{\mathrm{sb}} = \frac{C_1 - C_2}{C_1 + C_2} U_{\mathrm{rf}} . \qquad (1.24)$$

If the excitation frequency $\omega$ is small compared to other time scales, e.g electron and ion plasma frequencies, the electron current from the sheath $j_{\mathrm{L}}$ becomes bigger than the displacement current $j_{\mathrm{dc}}$. Hence the electron current onto the driven electrode decreases by a maxwellian



**Figure 1.3**: Schematic course of the voltage $U(t)$ and plasma potential $\Phi(t)$ for a directly and capacitively coupled rf discharge. Different cases of symmetry are shown: enlarged driven electron, grounded electrode and a symmetric discharge. [13]

factor — this is a function of the thereon apllied voltage — compared to the corresponding ion current. Conclusively, the electrodes sheath impedance is bigger than those of the floating walls. Together with equation 1.22 and equation 1.16 the plasma potential $\Phi_\mathrm{p}$ approximately vanishes, requiring only the currents onto the driven electrode to equal out. For small values of $\omega$ equation 1.25 yields the *self bias voltage* [13]. Here, $\mathbf{I}_0$ denotes the zeroth order modified *Bessel function.*

$$U_\mathrm{sb} = \frac{k_\mathrm{B}T_\mathrm{e}}{e} \ln \left[ \mathbf{I}_0 \left( \frac{eU_\mathrm{rf}}{k_\mathrm{B}T_\mathrm{e}} \right) \right] \tag{1.25}$$

## 1.1.5 Dielectric Displacement Current

Due to their higher mobility and plasma frequency $\omega_\mathrm{p,e}$, the electron distribution can follow an external excitation with a similarly high frequency much better than the heavier ions species. Because of that, one will assume those as nearly stationary, e.g. $\omega_\mathrm{p,i} \ll \omega_\mathrm{p,e}, \omega_\mathrm{rf}$. Investigating the circumstances and consequences of this relation yields the displacement current $j_\mathrm{d}$.

Lets suppose there is an area of thickness $d$ in front of a negatively charged wall, where the electron ensity is negligible and the corresponding ion property constant at $n_{0,\mathrm{i}}$. Thus an electric field of

$$E_0 = -en_{0,\mathrm{i}}d/\varepsilon_0 \tag{1.26}$$

establishes. If the wall potential now decreases due to electron bombardment or external manip-
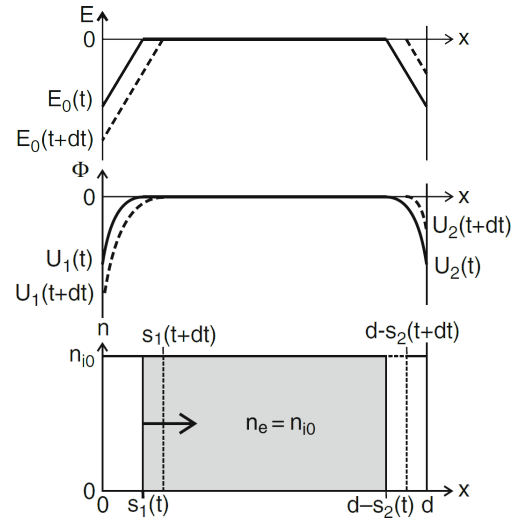


**Figure 1.5**: One dimensional density, potential and electric field for an asymmetric, harmonically driven discharge. Note the moving sheaths border. [13]

ulation, the sheaths border moves further inside into the discharges volume with the velocity $u_\mathrm{s} = \mathrm{d}s_1/\mathrm{d}t$. Thus, the sheath expansion and hence charge movement creates an additional *displacement current* $j_\mathrm{d}$, which is compensated with $j_\mathrm{d,e}$ the electron current from this border displacement. Hence charge conservation and continuity is satisfied [3].

$$j_\mathrm{d} = -en_{0,\mathrm{i}}u_\mathrm{s} = -j_\mathrm{d,e} \tag{1.27}$$

Electrons that are pushed out of this positive space-charge area then contribute to the plasma bulk density, and conclusively, to the quasi neutrality $n_\mathrm{e} = n_{0,\mathrm{i}}$. But in case of a harmonically driven discharge, the sheath in front of the opposing electrode is shrinking with $\mathrm{d}s_1 = -\mathrm{d}s_2$. Hence, the bulks spatial expansion and position are oscillating sinusoidal, or: the sheaths thickness oscillates harmonically around a mean value, e.g $s_0$. The associated voltage drop across the discharge [13] between the sheath potentials $U_{1/2}$ would be

$$\Delta U = U_1 - U_2 = -\frac{2en_{\mathrm{i},0}s_0}{\varepsilon_0} \exp\left(\mathbf{i}\omega t\right) \tag{1.28}$$

## 1.1.6   Heating Mechanisms

**Ohmic Heating**   In a spatially uniform electric field that oscillates perpendicular to the electrodes harmonically, like it is the case in the bulk of a previously concerned ccrf discharge, electrons periodically gain and loose energy in the absence of collisions without any net energy gain [15]. This is due to the symmetrical de-/acceleration in the sheaths an main plasma volume over one rf cycle. Lets assume the electric field have no or a negligible component parallel to the electrodes. Hence the mean absorbed power by the electrons in an oscillating electric field is

$$\overline{P}_{\mathrm{ohm}} = \omega_{\mathrm{rf}} \int_0^{T_{\mathrm{rf}}} j_{\mathrm{tot}}(t) \cdot E(t)\mathrm{d}t \qquad (1.29)$$

$$m_{\mathrm{e}} \frac{\mathrm{d}v_{\mathrm{e}}}{\mathrm{d}t} = -eE(t) - m_{\mathrm{e}}\nu_{\mathrm{n,e}}v_{\mathrm{e}} \qquad (1.30)$$

The total charge current density $j_{\mathrm{tot}}$ is the sum of displacement current from section 1.1.5 and conduction current $en_{\mathrm{e,0}}v_{\mathrm{e}}$. Solving equation 1.30 for the velocity, one yields and imaginary and real part due to the bulks impedance, like it was discussed earlier in section 1.1.4. Substitution of this result [15] gives

$$\overline{P}_{\mathrm{ohm}} = \frac{|E_0|^2 \operatorname{Re}(\sigma_{\mathrm{p}})}{2} = \frac{|j_0|^2}{2\operatorname{Re}(\sigma_{\mathrm{p}})} \,, \qquad \sigma_{\mathrm{p}} = \frac{n_{\mathrm{e}}e^2}{m_{\mathrm{e}}(\nu_{\mathrm{n,e}} + \mathbf{i}\omega_{\mathrm{p}})} \qquad (1.31)$$

This is, again, the total mean power dissipated into the electron species through acceleration in a harmonically oscillating electric field and neutral gas friction. The property $\sigma_{\mathrm{p}}$ is the plasma conductivity, hence yielding $j_0 = \sigma_{\mathrm{p}}E$. This shows that power from an spatially uniform, harmonically oscillating electric field can only be transferred via collisions. Elastic electron-neutrals collision transferred into a direction perpendicular to the field and is, hence, not lost during the reversal of $E(t)$. Therefore the electron species gains energy during the field oscillation. This mechanism is called *ohmic heating* and takes place mainly in the plasma bulk.

**Stochastic Heating**   Low-pressure, capacitively coupled rf plasma can primarily be stabilized by collisionless heating in the sinusoidally modulated discharge sheaths, like it was proposed earlier in section 1.1.2.1 and the following. Most theoretical models assume a 'hard wall' approximation (HWA), where the electrons are considered to collide elastically with the oscillating sheath edge. Heating power is then averaged by reverse and forward energy fluxes into and out of the sheath respectively. This gives an easy access to heating mechanisms of the proposed discharges.
The heating mechanism in such low pressure plasma is of particular importance, because collisions are rare and sheath processes are key to the sustainability of the discharge (see e.g section 1.1.3). The afore-mentioned HWA uses the '*fermi acceleration*' argument, which implies that the particles are heated or cooled due to the sheaths sinusoidal oscillation and a corresponding de-/acceleration. This process, though relying on enough randomization in phasespace inside the bulk, sufficiently creates a net heating of the plasma [5, 4]. This is referred to as *stochastic heating*.
Here one will consider the sheaths electric field as constant, $E = U_{\mathrm{sb}}/s_0$, the bulks expansion to be $l$ and the sheaths thickness $d$ being modulated cosinusoidal. The equation of motion for an

electron in the sheath is taken from above, cancelling out the part of ohmic neutral gas heating.

$$d(t) \approx s_0 \left(1 + \frac{U_{\mathrm{rf}}}{U_{\mathrm{sb}}} \cos(\omega t)\right) \tag{1.32}$$

The equation 1.30 is introduced to be dimensionless with the substitution of the corresponding parameters: $\alpha = m_{\mathrm{e}} \omega^2 s_0^2/(e U_{\mathrm{sb}})$, $\beta = U_{\mathrm{rf}}/U_{\mathrm{sb}}$ and $\epsilon = s_0/l$. Integration yields the velocity $\mu(\tau)$ of an electron as it moves through the sheath. The transit time $\tau$ is considered for one pass through the sheath of the particle. It can be used to calculate the change in velocity experienced by the electron on each bounce between this oscillating and a fixed wall — this would be the lowest order *fermi acceleration*. Assuming there are two distinct points in motion, where the particle enters (index $n$) and re-enters (index $n + 1$) the sheath, this gives, using $\varphi_{\mathrm{n}}$ the phase of the sheath, for the transit time and velocity [4]

$$\tau_{\mathrm{n}} \approx \frac{2\alpha(\mu_{\mathrm{n}} - \beta \cos \varphi_{\mathrm{n}})}{1 + \alpha\beta \cos \varphi_{\mathrm{n}}} , \qquad \mu_{\mathrm{n}+1} = -\mu + \frac{2(\mu_{\mathrm{n}} - \beta \sin \varphi_{\mathrm{n}})}{1 + \alpha\beta \cos \varphi_{\mathrm{n}}} \tag{1.33}$$

In *hamiltonian mappings*, those two variables are not canonically conjugate, hence insufficient for checking conserved quantities. One has to keep that in mind when evaluating the HWA approximation. The change in velocity in one pass through the sheath becomes the impulse approximation of the *Fermi acceleration*. Here, written again with common variables.

$$\Delta v = v_{\mathrm{n}+1} - v_{\mathrm{n}} = -2 \omega s_0 \frac{U_{\mathrm{rf}}}{U_{\mathrm{sb}}} \sin \varphi_{\mathrm{n}} \tag{1.34}$$

A question to answer is what parameter defines the degree of randomization required for an ample stochastical heating in the plasma sheath. Therefore, $K$ is defined as a function of phase-space chaos by electron energy. Additionally, a simple condition for stochastical motion is derived at the same time.

$$K = \alpha \beta \frac{U_{\mathrm{sb}}}{\epsilon E} , \qquad E < m_{\mathrm{e}} \omega^2 s_0 l \frac{U_{\mathrm{rf}}}{U_{\mathrm{sb}}} \tag{1.35}$$
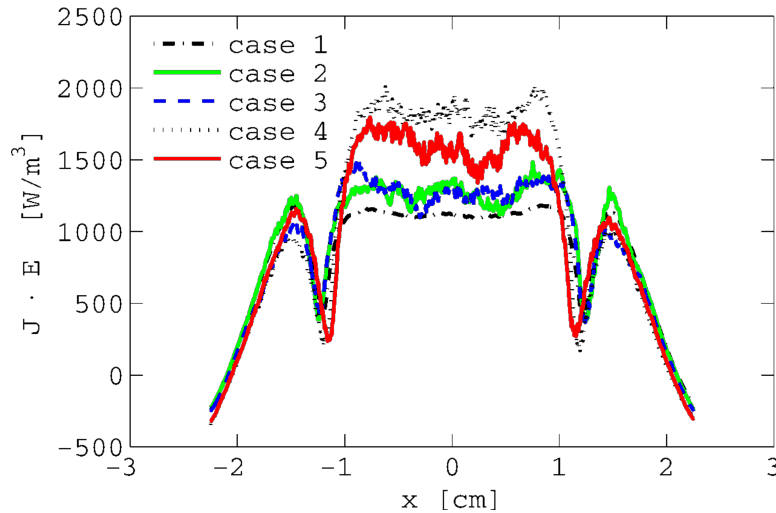


**Figure 1.6**: Electron heating rate for a ccrf discharge of parallel plates at 6.7 Pa with an electrode gap of 4.5 cm at 222 V. Other corresponding plasma parameters are noted in table 1.1. [6]

| Case | $\Phi_0$ | $n_{e,0}/m^{-3}$ | $n_{i-,0}/m^{-3}$ | $n_{i+,0}/m^{-3}$ | $T_{e,0}/eV$ |
|------|------|------|------|------|------|
| 1 | 101.30 | $2.43 \times 10^{14}$ | $1.17 \times 10^{16}$ | $1.20 \times 10^{16}$ | 2.83 |
| 2 | 101.25 | $2.29 \times 10^{14}$ | $1.21 \times 10^{16}$ | $1.23 \times 10^{16}$ | 2.98 |
| 3 | 101.75 | $2.18 \times 10^{14}$ | $1.19 \times 10^{16}$ | $1.20 \times 10^{16}$ | 2.98 |
| 4 | 103.11 | $1.55 \times 10^{14}$ | $1.75 \times 10^{16}$ | $1.78 \times 10^{16}$ | 3.59 |
| 5 | 102.55 | $1.65 \times 10^{14}$ | $1.70 \times 10^{16}$ | $1.71 \times 10^{16}$ | 3.43 |

**Table 1.1**: Selected plasma parameters for the used cases in figure 1.6 at the center of the discharge. [6]

As is well known [4], chaotic motion occurs in this mapping for $K > 1$. It decreases with increasing energy, so the system is less stochastic at higher energies. This is due to the shrinking phase shift across the discharge volume with higher energies. Hence phase correlations between successive collisions in and with the plasma sheath reduce stochasticity.

Last, but not least, one calculates the instantaneous power dissipated into the plasma due to this heating mechanism. Here, using the sheath speed from above $u_s$, the electron drift velocity $u_e$ and the maxwellian electron velocity distribution function $f_v(v_e, t)$, Lieberman [10] finds

$$P_{stoc}(t) = -2m_e \int_{u_s}^{inf} u_s(v_e - u_s)^2 f_v(v_e, t) dv = 2\,n_{e,0}u_e k_B T_e \sin(\omega t) \qquad (1.36)$$

Clearly, this results yields not net heating if averaged over one rf cycle. That is, if the current used would be conserved in a manner the HWA is predicting it, or the electron drift velocity does not satisfy the maxwellian distribution function. Hence, there have to be deviations from the proposed theory of stochastical heating. This would be e.g. ab initio information about the EEDF, unconsidered transit time effects of the sheath electric field and neglected particle losses and current conservation.

There are more theoretical approaches on the heating in low-pressure, low-temperature rf plasma. For example, Surendra et al [16] put forth the idea that the compression and de-compression of the electron density volume between opposing plasma sheaths generates heat inside the bulk is responsible for the observed heating.

The electron heating profile is shown in figure 1.6. The electron heating peaks near the sheath edges are due to the stochastic heating while the main plateau in the bulk is a result of the dominantly strong ohmic heating with slow electrons and neutral gas friction.

## 1.2   Oxygen Plasma Chemistry

In comparison to most inert working gases in ccrf discharges, oxygen has an overwhelming number of reaction sets for collisions of elastic, inelastic and reactive character. Additionally, the negative ion species has to be taken into account when discussing collisional processes. For example, an in-depth benchmarking of both simulated and experimentally measured cross section data is given by Gudmundsson et al. in [6]. There, 33 collisions and reactions have been revisited, already reducing the investigation to the most important processes in ccrf plasma. In this thesis the selection of possible reactions will be based on [1] and slightly modified. The final collection of cross sections can be found in table 1.2 and observed in figure 1.7. Those data are

semi-empirical, meaning part of them are based on measurements in finite energy ranges and low-/high-energy asymptotic models. Cross sections for very high energies are not important, as the collision probability usually decays very fast here.

As already seen in section 1.1.6, collisions strongly influence the particle distribution functions and density profiles. Furthermore, a good understanding of the plasma chemistry is key to, e.g. applications in surface physics supported by gas discharges. Of high importance for plasma-assisted material processes is the generation of negative ions. Hence the ratio $\alpha = n_{i,-}/n_e$ is important to characterize the electronegative plasma, like a ccrf oxygen discharge by $\alpha > 1$.

I will highlight the most important collisions and reactions in the following section.

| Nr. | Reaction | Type |
|-----|----------|------|
| | **Elastic scattering** | **Energy loss** |
| (1) | $e^- + O_2 \rightarrow O_2 + e^-$ | |
| (2) | $O^- + O_2 \rightarrow O_2 + O^-$ | |
| (3) | $O_2^- + O_2 \rightarrow O_2 + O_2^-$ | |
| | **Electron energy loss scattering** | **Energy loss** |
| (4) | $e^- + O_2 \rightarrow O_2^\nu + e^-$ | Vibrational excitation $(\nu = 1, \ldots, 4)$ |
| (5) | $e^- + O_2 \rightarrow O_2(Ryd) + e^-$ | Rydberg excitation |
| (6) | $e^- + O_2 \rightarrow O(1D) + O(3P) + e^-$ | Dissociative excitation at 8.6 eV |
| (7) | $e^- + O_2 \rightarrow O_2(a^1\Delta_g, b^1\Sigma_g)$ | Meta-stable excitaion |
| | **Electron and ion reactions** | **Creation and loss** |
| (8) | $e^- + O_2^+ \rightarrow 2O$ | Dissociative recombination |
| (9) | $O^- + O_2^+ \rightarrow O_2 + O$ | Neutralization |
| (10) | $e^- + O_2 \rightarrow O + O^-$ | Dissociative attachment |
| (11) | $O^- + O_2 \rightarrow O + O_2 + e$ | Direct detachment |
| (12) | $e^- + O_2 \rightarrow 2e^- + O_2^+$ | Impact ionization |
| (13) | $e^- + O^- \rightarrow O + 2e^-$ | Impact detachment |

**Table 1.2**: Most important colilision and reactions in ccrf plasma with the largest cross sections. Empirical and simulated data, which have been included in this simulation are shown in figure 1.7.

### 1.2.1 Collisions and Reactions

**Elastic Scattering**  The elastic collisions of (1)–(3) conserve the particle numbers. Those are inter-species scattering processes, which will be assumed to have an isotropic inincident angle dependency [1]. Intra-species elastic collisions were not very important at the selected parameter regions, though ion-ion scattering can strongly incluence the IEDF structure of the concerned densities are very high. However, for the electron species a binary *coulomb scattering* process was used: the scattering angle $\chi$ is given by equation 1.37 with $v_{rel}$ the relative velocity, $\ln\Gamma$ the Coulomb logarithm (see table A.1) and $\tau_c$ the collision time.

$$\langle \tan^2 \frac{\chi}{2} \rangle = \frac{e^4 n_e \ln\Gamma}{8\pi\varepsilon_0 m_e^2 v_{rel}^3} \tau_c \tag{1.37}$$

The figure 1.7 shows the corresponding cross sections. In fact, only two are elastic processes, where as the collision of $O_2^+$ and the neutral molecule is a charge exchange reaction with momentum transfer. This kind of process:

$$A^{-/+} + B \rightarrow A + B^{+/-} \tag{1.38}$$

is important for the consideration of surface effects. An ion with greater than thermal velocity coming from the wall will be cooled down by charge exchange collisions, which will transfer heat into the neutral reservoir.

**Electron Energy Loss**   Electron energy loss occurs due to inelastic collisions (4)–(7), where an oxygen molecule is excited or dissociated into fragments. Here, the spatio-temporal evolution of the molecule or the fragments are of no interest for this thesis. Hence they are treated as 'test collisions', in which only the electrons lose momentum and change direction. Again, the neutral particle reservoir is considered to equilibrate at a sufficiently short time scale $< 10^{-15}\,\mathrm{s}$. Rotational excitations are found to be unimportant, though the vibrational parts considerably influence the EEDF [6]. The isotropic post-collision relative velocity change in the center-of-mass system gives

$$\widetilde{v}_{\mathrm{rel}} = \sqrt{v_{\mathrm{rel}}^2 - \frac{2\Delta E}{\mu_{\mathrm{i,j}}}}\,. \tag{1.39}$$

The most important electron energy loss scattering is the vibrational and electronic excitation, as well as the dissociation of the oxygen molecule.

**Electron and Ion Channels**   The last class of collisions concerned here are the electron and ion production processes. Collisions (8) and (9) are the annihilation of the two oppositely charge particles. Those are namely recombination processes. The ion-ion neutralization is constructed by a *Landau-Zener* model, where the adiabatic energy of the $(O^-,O_2^+)$ configuration decreases when the particles approach each other. At the critical distance $R_{\mathrm{c}}$ this energy drops bellow the one of the $(O,O_2)$ configuration, yielding the probability to change states $\sigma_{\mathrm{r}}(E)$

$$\sigma_{\mathrm{r}}(E) = 4\pi R_{\mathrm{c}}^2 \left(1 + \frac{1}{R_{\mathrm{c}}E}\right)\,. \tag{1.40}$$

The dissociative attachment (10) and direct detachment (11) are treated as binary collisions, like the elastic electron scatter process. For the dissociative attachment from the ground state oxygen molecule a threshold energy of $4.2\,\mathrm{eV}$ is needed. The incident electron loses this energy to the $O_2^-$, which afterwards breaks up into the two fragments. The electron transition time is, again, assumed to be short on a nuclear timescale and the resulting particles share the remaining kinetic energy of the incident electron.

In the experiment there is a second stage for the direct detachment process: through associative detachment, oxygen atom, electron and molecule form an ozone $O_3$ particle. This most likely due to the presence of meta-stable $O_2(a^1\Delta_{\mathrm{g}})$. After the necessary threshold energy of $1.3\,\mathrm{eV}$ has been supplied to directly detach $O^-$ on an oxygen molecule, the afore-mentioned detachment takes no energy whatsoever, making it a potentially important loss channel for cold $O^-$ ions.

For impact ionization (12) and detachment (13) the following is assumed: first, an inelastic binary collision takes place, in which the electron loses the necessary reaction energy. The

post-collision oxygen particle is afterwards split into an additional $e^-$ and atom/ion ($O^-/O$), which proceed to perform an elastic binary collision. During this process, energy and momentum conservation is satisfied, ensuring numerical stability.

## 1.2.2   Anion Species

The main production channel of negative oxygen ions in ccrf disharges at low pressures and temperatures is the dissociative attachment reaction (10). Here, an electron becomes attached to a molecule. The successive electronic excitation is of short duration and does not change the intra-molecular distance. Afterwards, theres a significant chance of transition to a dissociative state exists, which has a lower equilibrium energy at greater intra-nuclear distances. Hence, the dissociation of this molecule is rather likely.

$$e^- + AB \rightarrow A + B^- \tag{1.41}$$

Another possible creation channel is a three-body collision of non-dissociative character, whose cross sections is magnitudes smaller than the one of equation 1.41. Hence I will only consider dissociative attachment reactions (10) for the anion production.

Negative ion loss can happen through reactions (11), (13) and (9). The latter is the only collision with a cross section larger than the creation via dissociative attachment (see figure 1.7). For all relative energies, the neutralization has a probability of at least one magnitude larger than the other channels. Cross sections of direct (11) and impact (13) detachment are, depending on the energy, about one to two orders of scale smaller.
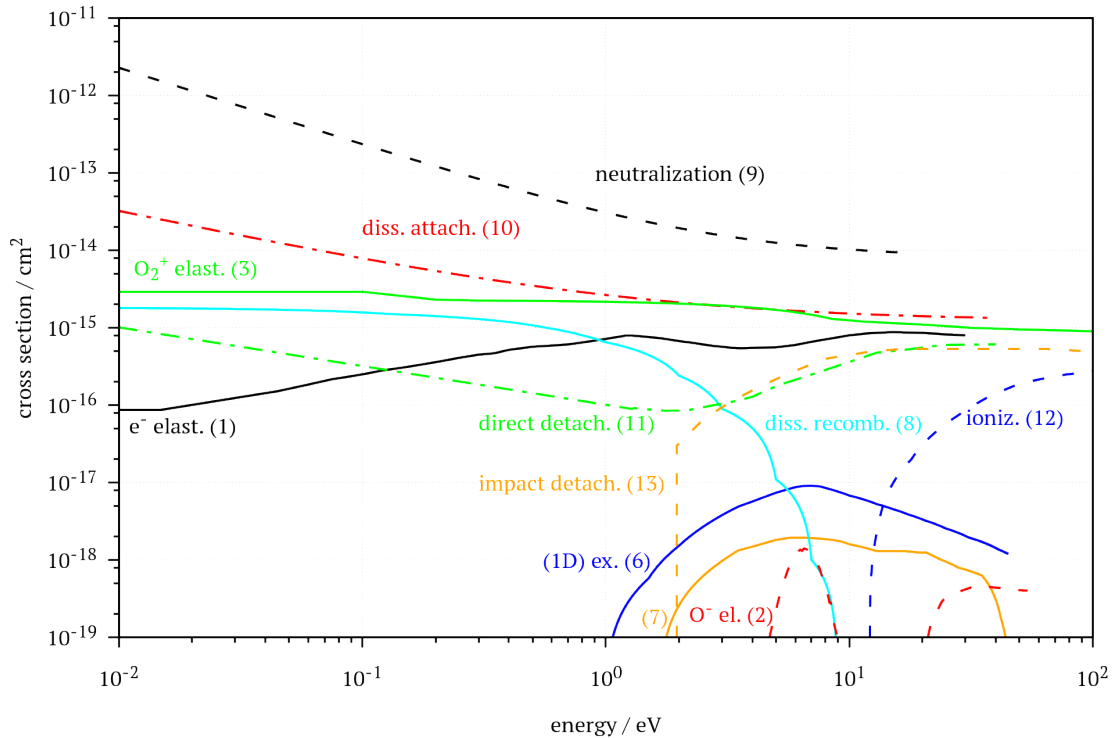


**Figure 1.7**: Cross section data of electron energy loss, electron and ion production/loss and elastic scattering collisions from [6] and [1]. The corresponding reaction equations are shown in table 1.2.

In general, the produced negative ions are cold. The anion distribution reaches until the boundaries of the bulk, where processes with large cross sections at low energies become important [1]. Those reactions would be ion-ion neutralization and associative detachment. Direct detachment, though being still present around $E < 1\,\text{eV}$, has an energy threshold and is not significant for this region. Furthermore, the probability of neutralization (9) is proportional to the $O_2^+$-density. Bronold et al. proposes, that the production and loss of $O^-$ is rather insensitive to voltage changes up to $300\,\text{V}$. Furthermore, the most important range for incident energies will be 4–15 eV, while the EEDF is rather voltage-independent.

Considering the physics of a negative ion — $O^-$ follows the same dynamic and kinetic behaviour as the electrons, but is easily confined by the plasma potential due to their much greater mass and, hence $\omega_{p,i-} << \omega_{p,e}$ — the main loss and production channels are most prominent in the bulk. Therefore, a low-pressure, low-temperature ccrf discharge has an electronegative core, in which the cold anions are captured, and areas where they are excluded. The presence of negative ions also has a great impact on the distribution functions of other plasma species. It is possible to form a quasi-neutral volume core, consisting only of ion species, and a peripheral electron-ion plasma in the discharge sheaths. At pressures $> 30\,\text{Pa}$ and large input powers, the value of electronegativity $\alpha$ leads to instabilities between ionization and electron attachment reactions. The electron density peaks, where as the corresponding temperatures drops. Because of the strong negative ion coupling, the $O^-$ density fluctuates as well.

## 1.3    Particle-in-Cell Simulations with Monte Carlo-Colissions

Particle-In-Cell simulations with Monte-Carlo-Collisions (PIC-MCC) represent a powerfull tool for fully kinetic, high-dimensional plasma studies, with inclusion of complicated reaction/collision routines, as well as field solving methods. Hence they are used in all branches of plasma physics, ranging from simple labratory discharges to electro-propulsion ion-thrusters and interplanetary astrophysical system. This kind of computer code simulates the motion of up to $10^{10}$ individual particles, though this limit is only due to the available fast cache memory on the system side, in a continous 1d3v-/2d3v phase-space. Macro-quantities like forces, fields and densities are stored and calculated on a strict mesh scheme with fixed intervals. The computational cost sums up to $N\log(N)$ per timestep — with $N$ the total particle number — because the self-consistent electrostatic macro-fields are calculated globally by the *Poisson's equation*, and no particle-particle interactions are considered.

In the following section the motivation and basic scheme of a PIC-MCC simulation will be highlighted. Accordingly, the collion routines will be layed out, as well as the transition from a 1d3v to 2d3v model. As it was mentioned in chapter 1, the focus of this thesis is on unmagnetized plasma. The magnetic field generated from the moving charged particles is small enough that the force of $q_j(\vec{v}_j \times \vec{B})$ is negligible in comparison to $q_j\vec{E}$.

### 1.3.1    Principles

In general, the spatio-temporal evolution of the velocity distribution function $f_j(\vec{v}, \vec{r}, t)$ is given by the *Boltzmann equation*:

$$\frac{\partial f_j}{\partial t} + \vec{v} \cdot \nabla_{\vec{r}} f_j + \frac{q_j}{m_j}\vec{E} \cdot \nabla_{\vec{v}} f_j = \left(\frac{\partial f_j}{\partial t}\right)_{\text{Coll}}. \tag{1.42}$$

In this equation, the product of $q_\mathrm{j}\vec{E}/m_\mathrm{j}$ denotes the electrostatic force onto the particle of species $j$. The velocity and space gradient are calculated like $\nabla_{\vec{r}} f_\mathrm{j} = \partial f_\mathrm{j}/\partial x \cdot \vec{e}_\mathrm{x} + \ldots$ and so on. The right hand side of $(\partial f_\mathrm{j}/\partial t)_\mathrm{Coll}$ is the sum of all collisional effects on $f_\mathrm{j}(\vec{v}, \vec{r}, t)$. An approach would be an integral form, in which all probabilities of a two-body interactions with different incident and outgoing velocities are summed up in a *Faltung integral* with $f_\mathrm{j}(\vec{v}, \vec{r}, t)$. The approach via the distribution function yields the advantage of an easy access to the afore-mentioned macro-quantities, the zeroth and first moment are noted below in equation 1.43. Using the moments, one can write down $f_\mathrm{j}(\vec{v}, \vec{r}, t)$ at a thermodynamical equilibrium of $T_{\mathrm{j},0}$ as the *Maxwell-Boltzmann-distribution-function* in equation 1.44.

$$n_\mathrm{j}(\vec{r}, t) = q_\mathrm{j} \int_{-\infty}^{\infty} f_\mathrm{j}(\vec{v}, \vec{r}, t)\mathrm{d}\vec{v}, \qquad \langle v_\mathrm{j}(\vec{r}, t)\rangle = \frac{1}{n_\mathrm{j}(\vec{r}, t)} \int_{-\infty}^{\infty} \vec{v} f_\mathrm{j}(\vec{v}, \vec{r}, t)\mathrm{d}\vec{v} \qquad (1.43)$$

$$f_\mathrm{j}(\vec{v}, \vec{r}, t) = \frac{n_\mathrm{j}(\vec{r}, t)}{q_\mathrm{j}} \hat{f}_\mathrm{j}(\vec{v}, \vec{r}, t) = \frac{n_\mathrm{j}(\vec{r}, t)}{q_\mathrm{j}} \left(\frac{m_\mathrm{j}}{2\pi k_\mathrm{B} T_{\mathrm{j},0}}\right)^{3/2} \exp\left(-\frac{|\vec{v}_\mathrm{j}|^2}{v_{\mathrm{j,th}}^2}\right) \qquad (1.44)$$

In a maxwellian distributed plasma at an equilibrium, one could use a fluid dynamic approach, where the equations of motion for a single particle are multiplied with the number density function. This would reduce the computational cost drastically, as one would no longer have to track each particle individually, and sufficiently describe the discharge by charaterization of macro-quantities. This is true, if mean-free-paths are small and collisions rather likely, hence the afore-mentioned distribution function correct. In a low-temperature, low-pressure ccrf discharge mean-free-paths are large and collisions happen infrequently, which is why a Particle-in-Cell simulation method is used.

Satisfying the above requirements, the *n*-th equation of motion in the *N*-particle system becomes:

$$\frac{\mathrm{d}\vec{x}_\mathrm{n}}{\mathrm{d}t} = \vec{v}_\mathrm{n}, \qquad \frac{\mathrm{d}\vec{v}_\mathrm{n}}{\mathrm{d}t} = \frac{1}{m_\mathrm{n}} \vec{F}_\mathrm{n,L}(\vec{x}_\mathrm{n}, \vec{E}, t) = \frac{q_\mathrm{n}}{m_\mathrm{n}} \vec{E}(\vec{x}_\mathrm{n}, t) \qquad (1.45)$$

where $F_\mathrm{n,L}$ is the *electrostatic Lorentz force*.

First, the global charge density is calculted by interpolating the point charges $q_\mathrm{n}$ of each particle onto the afore-mentioned fixed mesh grid ( equation 1.46 ). Next, the Poisson's equation is solved globally on that grid ( equation 1.47 ), using the interpolated density. At last, the Maxwell'is equation 1.48 yields the electric field.

$$\rho(\vec{r}, t) = \rho(\vec{x}_1, \vec{x}_2, \ldots, \vec{x}_\mathrm{N}, t) \qquad (1.46)$$

$$\Rightarrow \Delta\Phi(\vec{r}, t) = -\frac{\rho(\vec{r}, t)}{\varepsilon_0} \qquad (1.47)$$

$$\Rightarrow \vec{E}(\vec{r}, t) = -\nabla\Phi(\vec{r}, t) \qquad (1.48)$$

The number of *N* is of orders of magnitude higher than what the best supercomputers can handle. Hence it is assumed that one simulated particle at $\vec{x}_\mathrm{n}$ and veloctiy $\vec{v}_\mathrm{n}$ represents many physical particles. This *superparticle factor* is usually between $10^3$–$10^4$, depending on the size and initial density in the simulated domain. Those superparticles follow the same dynamic and kinetic behaviour like their physical counterparts, assuming that all other relevant parameters are scaled accordingly.

Like the domain composition and field mesh grid, the time is divided into discrete time steps, which yields the simulation time $t \to t_\mathrm{k} = t_0 + k\,\Delta t$ (and correspondingly all other physical properties). Here, a *leap frog* method is used to calculate the velocities, in contrast to other

time-dependent attributes, which still satisfies the needs of accuracy, short computational times and stability. With each calculation step, the error scales with $\sim \Delta t^2$ and fulfills the requirement for numerical stability $\Delta t^{\alpha>1}$. The explicit leap frog solution is calculated with old quantities of the previous timestep, thus it is simpler and faster. The single drawback on this method would be the requirement of a smaller timestep, e.g $\Delta t/2$.

The most significant part of the simulation code is the *particle mover* or *particle pusher*, in which the equation of motions are discretised and the new positions and velocities calculated. For each particleof index $n$ and species $j$ the following equations have to solved at a given time step $k$, or $k+/-\frac{1}{2}$ respectively:

$$\vec{u}_{n,+} = \vec{v}_{n,k\text{-}1/2} + h \cdot \vec{E}_k \,, \qquad h = \frac{q_j}{2\,m_j}$$

$$\boxed{\vec{x}_{n,k+1} = \vec{x}_{n,k} + \Delta t \vec{v}_{n,k+1/2} \quad \text{and} \quad \vec{v}_{n,k\text{-}1/2} = \vec{u}_{n,+} + h \cdot \vec{E}_k} \qquad (1.49)$$

The field, potential and density only have to be calculated once per time step. Though this requires less effort, the calculation of $\vec{E}$, $\Phi$ and $\rho$ need to be done by one processing core. The equation equation 1.46 and following are solved globally. For example, the Poisson's equation for a two-dimensional, with $\Delta r$ equally grided mesh at $(r_l^{(1)}, r_m^{(2)})$ in a discrete form becomes the *five point star equation*:

$$4\Phi_{l,m} - \Phi_{l\text{-}1,m} - \Phi_{l+1,m} - \Phi_{l,m\text{-}1} - \Phi_{l,m+1} = \Delta r^2 \cdot \frac{\rho_{l,m}}{\varepsilon_0} \qquad (1.50)$$

While the updated field, potential and density are calculated, all but one processing core remain idle and wait for the result to be distributed and used in the particle pusher in equation 1.49. The universal stability criteria for a kinetic plasma simulation using a PIC method with a twodimensional, spatial mesh size $\Delta r$ and time step $\Delta t$ are given by equation 1.51. The spatial and temporal step width should sufficiently resolve the smallest and fastest processes in the simulated model. Hence the physical scales of electron plasma frequency $\omega_{p,e}$ and Debye length $\lambda_D$ are chosen. For example, an electron never flies beyond one Debye cell during a single step of time. Also the interpolation of the macro-quantities yields an error the size of micro-fluctuations between single particles, thus is negligible.

$$\boxed{\Delta t_0 \leq 0.2 \cdot \omega_{p,e} \quad \text{and} \quad \Delta r_0 \leq 0.5 \cdot \lambda_D} \qquad (1.51)$$

To summarize this section, a basic simulation code cycle for one time step of a PIC-MCC method is shown in figure 1.8. A more versatile and in-depth approach on PIC or Cloud-In-Cell (CIC) simulations can be found in [17].

### 1.3.2   2d3v PIC

In the following, I will highlight the difficult tasks of a spatially twodimensional PIC simulation, refering to the scheme in figure 1.8.

**Discharge Setup**   In the beginning of the simulation, before the first calculation step is done, the domain has to be constructed. The cylindrical setup is reduced to the radial and axial dimensions, e.g $(r, z)$ for reasons of symmetry. The five-dimensional phase-space is completed with the full velocity triplet $\vec{v} = (v_r, v_z, v_\vartheta)$. Two onedimensional grids in radial and axial
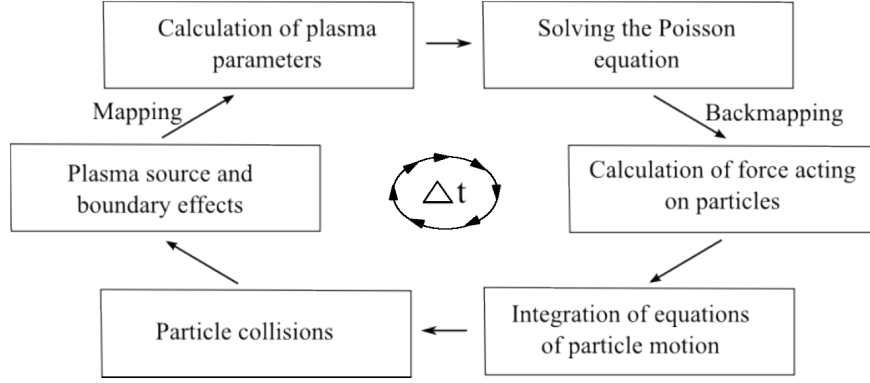
**Figure 1.8**: PIC simulation scheme [12]. The code starts with the initilisation of all particle species with their corresponding velocities and a first mapping process, followed by the solution of the Maxwell's equation equation 1.48. Afterwards the main loop with push, collisions, mapping and so on begins.

directions, with $N_r$ and $N_z$ equally sized partitions respectively, are layered over each other to form the final discharge domain. Hence, the are of a single mesh cell is $\Delta r_0^2$. The spatial and temporal discretisation $\Delta r_0$ and $\Delta t_0$ are chosen to be dimensionless, so calculations inside the code can be performed much more easily and are less likely to have errors.

Additionally, certain physical properties have to be scaled according to the spatial weight of a cell. Because a 'quasi-three-dimensional' cell of coordinates $(n_r, n_z)$ grows in volume with increasing radial index (for a more visual approach, take a look at figure 3.2), a weighting factor needs to be multiplied with properties like densities and pressure.

After the domain composition, the particle initialization is to be done. Here, one uses pressure and intial density to model a global distribution of electrons, ion and neutral species. The corresponding super particle factor is used to decrease computational time. Though it has been proven that this does not introduce artifacts to the simulations results — the equation of motion only depends on a charge-to-mass-ratio — it should not be too high. Collisions may be underrepresented when there are not enough targets, though in reality $\sim 10^4$ times the amount of particles would be available.

To initialize the particles, a number of electrons, ions and neutrals is ditributed in each cell, using a Maxwell-distribution-function. Inside one mesh unit the, e.g neutrals are spread continuosly and randomized. The same goes for the velocity, which is specified by the distribution function. The radial deformation of each cell has to be taken into acccount here. Therefore more particles have to be initiated in cells the closer they get to the outer limit of the cylindrical domain.

Now that $N$ particles have been ditributed equally in the simulated area, the computational workload is shared between the $M_{PC}$ processing cores. The domain is therefore decomposed in partitions of equal particle numbers, e.g $N/M_{PC}$. This speeds up the collisional and diagnostics routines, as each core only has to calculate on its own, but it does not reduce the time needed for the Maxwell's and Poisson's equation (see section 1.3.1).

**Potential and Field Calculation**   After the domain is filled and decomposed, the resulting density distribution, potential and electric field have to be calculated. The charges need to be mapped to the grid points to generate a density, which can be used by a discrete solver of the Poisson's equation (see equation 1.50). A linear weighting function is applied for each charge to form the density. The resulting scheme for a particle at $(r, z)$ in one and two dimensions
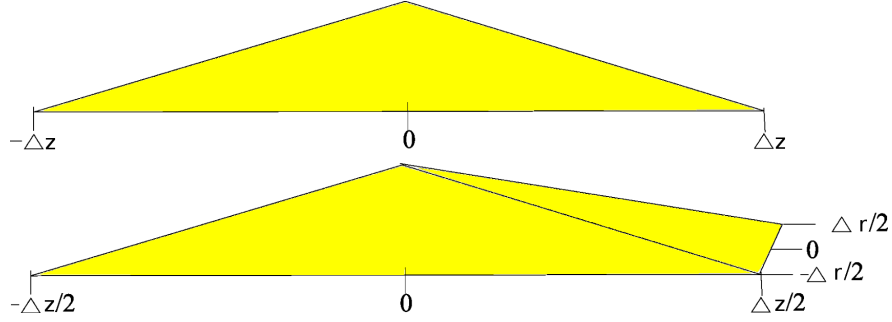
**Figure 1.9**: Linear weighting scheme for (top) 1D and (bottom) 2D simulations. The latter is an expansion into the radial dimension from a 1D case. The twodimensional approximation is called Cloud-In-Cell (CIC).

is shown in figure 1.9 and equation 1.53. The index tuple $k, j$ denotes the position in the twodimensional mesh, $n_{k,j}$ the corresponding density, $(r_k, z_j)$ the position — this e.g would be $r_k = \Delta r_0 \cdot k$ and so on — and $S_{k,j}$ the statistical weight, composed of dimensionless charge, super particle and volume factor. The quotient $A_{k,j} = \Delta r_0^2$ normalizes the result, so that no error is made when summarizing all four contributions of a single particle to the density.

$$1\text{D:} \qquad n_j = \frac{S_j}{\Delta z} \left( z_j - z \right) \tag{1.52}$$

$$2\text{D:} \qquad n_{k,j} = \frac{S_{k,j}}{A_{k,j}^2} \left( r_{k+1} - r \right) \cdot \left( z_{j+1} - z \right) \tag{1.53}$$

To avoid possible self-forces and satisfy the conservation of momentum, the same weighting method has to be used when back-mapping the calculated forces from the discrete grid points to the particle positions. Again, for a more detailed discussion see [17].

The discretised matrix equation of equation 1.50, and equation 1.47 respectively, is solved using a *LU-factorization*. For example, another method of matrix-solver would be the successive-over-relaxation (SOR). The potential is calculated every time step using this factorization, but the latter is done only once at the beginning, because it only depends on the mesh, and hence the composition of the matrix $\Phi \in \mathbb{R}^{N_r \times N_z}$. This is also the moment to apply any potential boundary conditions, such as external voltages $U_{rf}(t)$ or ground $\Phi = 0$.

The force resulting from equation 1.48 is again mapped back to the individual particle positions using the same scheme as equation 1.53 for the, with $\Delta r_0$ equally composed 2D-mesh. Therefore, momentum conservation is satisfied.

**Particle Pusher**

### 1.3.3 Monte Carlo-Collisions

# Chapter 2

# Validation of Simulation by 1d comparison

## 2.1 Axial density profiles

## 2.2 Velocity and energy distributions

## 2.3 Transition to 2d simulation

# Chapter 3

# Simulation of capacitively coupled rf discharges

## 3.1 Experimental setup

Giving the necessary background in section 1.1.2.2 and providing the crucially important comparison of the previous chapter 2, the afore-mentioned effects of highly energetic negative oxygen ions can now be further investigated.

### 3.1.1 Reference Discharge

Here, the referenced experiment was used by Küllig et al. [9] and Scheuer [14], and consists of a cylindrical setup, filled with oxygen at low pressures and gas flow rates (see figure 3.1). The stainless steel vacuum chamber had a diameter and height of 40 cm respectively and was filled with the process gas oxygen ($O_2$) at 5 sccm (**FC**). The discharge configuration consisted of an electrode in the center with 10 cm of diameter and a rf generator, constantly operating at a
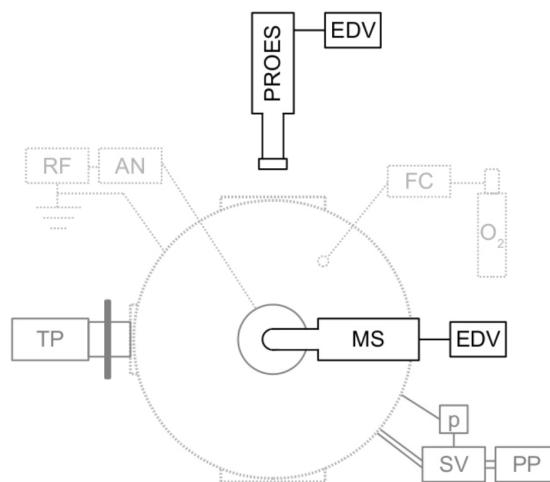


**Figure 3.1**: Top-down view schematic of the experiment [14], [9]. Shown is the setup without microwave interferometer, like it was used by Küllig et al.

frequency of 13,56 MHz and power outputs between 5 and 150 W (**RF** and **AN**), leading to applied voltages in the range of 100–1500 V. Shielding and discharge enclosure/chamber walls were grounded, therefore yielding a large area ratio between driven and grounded electrode and establishing a heavily asymmetric plasma. In addition, the powered electrode was coupled capacitively with the external generator, emphasizing the effect of the, in section 1.1.4 introduced self bias voltage. The value of $U_{\text{sb}}$ ranged, depending on power output and discharge pressure, from $-100$ up to 500 V. In [9] the experiment was pulsed with short discharges at a frequency of 10 Hz. Line integrated measurements resulted in an average electron density of around $10^{11}$–$10^{12}\,\text{cm}^{-3}$. Showing a schematic top-down view of the experiment is figure 3.1. Here, the large ratio between driven and grounded parts is very well visualized. Hence, in later simulations it will be of sufficient accuracy to restrain the virtualized volume to a smaller setup.

The figure below includes further diagnostics like a mass spectrometer (**MS**) and phase resolved optical emission spectroscopy (**PROES**). The latter measured the mentioned densities via line integration across the plasma volume. The MS is a key instrument for the investigation pursued in this thesis, as it also measures species counts with respect to their contribution to their correspoding energy distribution function. For example, the ions created via secondary processes in the discharge sheath are accelerated towards the bulk and thus get into the MS with their characteristic speeds and mass. A significant increase of electron density was found for rf powers larger than 50 W or $-220$ V self bias voltage [9]. This led to a correlating negativ oxygen ion density reduction and decrease of the electronegativity ratio $\overline{n}_{i,-}/\overline{n}_{\text{e}}$ from 4 to 0,03. During a different operation mode — called $\alpha$-mode, contrary to the afore-mentioned $\gamma$-mode — at less than 50 V output power, electronegativity rises again, as well as the electron temperature $T_{\text{e}}$, yielding higher rate coefficients for, e.g. dissociative electron attachment and the alike. See section 1.2.2 for a more detailed approach.

### 3.1.2   Simulated Discharge

All of the above conditions are sufficient for a practical approach at a labratory ccrf discharge with great repeatability. Though being highly optimized and developed over the course of many years, the twodimensional particle-in-cell code outlined above does not provide the tools and performance to feasibly simulate such large areas and particle numbers. Hence, one will reside to reducing the numerical expense by virtualizing smaller discharge areas and average densities, while trying to satisfy the same physical processes exhibited in [9].

The afore-mentioned 2d3v PIC code is used to simulated the referenced experiment. The spatial dimensions will be the radial component $r$ and axial coordinate $z$. The geometry and simulation is optimized for cylindrically symmetric gas discharges.

To represent the strong asymmetry between driven and grounded wall areas, the sizes of anode, cathode and grounded chamber parts have been chosing accordingly. The experimental values for the self bias voltage $U_{\text{sb}}$ were used to create a dc offset on-top of the rf voltage $U_{\text{rf}}$ at the cathode. The domain composition with cells of width $\lambda_{\text{D,e}}/2$ (see section 1.3.1) makes it even more difficult to appropriately model the system. Hence a smaller discharge volume of a 4,5 cm radius and an electrode gap of 2,5 cm will be simulated. This usually leads to cell counts up to $2 \cdot 10^5$, which is small in comparison to the 'real' experiment, which would have to be covered by over $10^6$ cells. Furthermore, the numerical expense grows with $N\log(N)$, and $N$ being the particle number inside the cells (see section 1.3).

One has chosen pressures between 2 Pa and 10 Pa, with the possibility of changing it later during

the discharges simulation — e.g to change the bulk volume and densities. The secondary ion emission efficiency was set to $\eta = 0{,}03$ in all cases, yielding a stable plasma sheath and hence SIE current into the bulk. In addition, a constant self bias of $-200\,\text{V}$ was appplied at the cathode. The radio frequency was set to $13{,}56\,\text{MHz}$.

The governing electron density and temperature were set to $5 \cdot 10^9\,\text{cm}^{-3}$ and $5\,\text{eV}$ respectively, which, as an initial value and property for scale, is sufficient for the necessary rate coefficients mentioned above. This led to the following important scales of simulation:

$$\lambda_\text{D} = 0{,}0235\,\text{cm}\,, \qquad\qquad \omega_\text{p,e} = 3{,}99 \cdot 10^9\,\text{Hz} \tag{3.1}$$

$$\Rightarrow \Delta x = \frac{1}{2}\,\lambda_\text{D} = 0{,}01174\,\text{cm}\,, \qquad \Delta t = 0{,}2 \cdot \omega_\text{p,e} = 5{,}015 \cdot 10^{-11}\,\text{s} \tag{3.2}$$

Thus a single rf cycle at the given frequency takes 1470 steps, and the domain measures 384 and 213 in radial and axial dimension respectively. An ion temperature is adjusted via the fraction $T_\text{i}/T_\text{e} = 0{,}008$, hence the corresponding velocities for the previously defined electron temperature $T_\text{e} = 5\,\text{eV} = 5{,}8 \cdot 10^4\,\text{K}$ are found to be

$$v_\text{th,e} = 9{,}37 \cdot 10^5\,\frac{\text{m}}{\text{s}}\,, \qquad c_\text{s,e} = 3{,}87 \cdot 10^3\,\frac{\text{m}}{\text{s}} \tag{3.3}$$

$$v_\text{th,i} = 558{,}38\,\frac{\text{m}}{\text{s}}\,, \qquad\quad c_\text{s,i} = 371{,}44\,\frac{\text{m}}{\text{s}} \tag{3.4}$$

Here, a single millisecond of operation takes days, if not weeks to simulate with a given timestep, like in equation 3.2. Due to this and the fact, that the unit cell volume increases with the layer index of the radial coordinate — one has to keep in mind that the cylindrical geometry is key to the simulation because important simplifications and assumptions inside the code itself are made uppon that premise —, each particle carries an additional statistical weight. For example, a virtual neutral gas molecule of $O_2$ may represents up to $10^8$ 'real' particles in a laboratory plasma. This saves a vast amount of computational time by immensely reducing the particle counts necessary to sufficiently model the investigated physical processes. In this case, a single neutral gas particle is statistically amplified by a factor of $\approx 9{,}3 \cdot 10^7$ to account for the gas density at $5\,\text{Pa}$ and $\approx 300\,\text{K}$. This number is crucial to all collisional processes, where the molecular species $O_2$ is involved. Charged particle species share a common number amplification of 8489. On top of both super particle factors, a scaling $\sim 1/r$ is applied to consider the variable cell volume.

Another numerical tool is a constant neutral gas background. In the afore-metioned experiment, a working gas reservoir and flow rate meter control the pressure and exchange of $O_2$ inside the chamber. Due to the slow transition velocities of the cold neutral species, a working gas current from e.g. behind an electrode is not feasible in this simulation. Collision rates and reaction coefficients are destroying neutral gas particles faster than they can be sufficiently supplied to the discharge. Hence, the $O_2$ molecules are initiated at time $t = 0$ of the simulation — this is done with respect to pressure, super particle factor and the
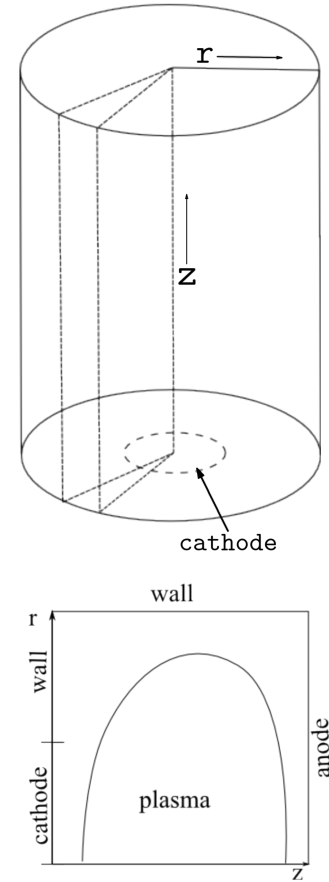


**Figure 3.2**: Simplified cylinder schematic for the simulated experiment. The slice depicte in the top is shown below. There, boundaries and bulk position are outlined.

alike —, and are afterwards not altered in number or location.
Though collision routines are still exercised, the corresponding
push of the neutral species is skipped.


## 3.2    Simulated ccrf Oxygen Discharge

In the collection of **??** twodimensional densities and potential are shown. Again, parameters
were chosen as $U_{\mathrm{rf}} = 400\,\mathrm{V}$, $p = 5\,\mathrm{Pa}$ and the initial species attributes to be $T_{\mathrm{e}} = 5\,\mathrm{eV}$,
$n_{\mathrm{e},0} = 5 \cdot 10^9\,\mathrm{cm}^{-3}$ and $T_{\mathrm{i}}/T_{\mathrm{e}} = 0{,}008$ respectively.


## 3.3    Anion Energy Distributions in Oxygen

# Chapter 4

# Conclusion

# Appendix A

# Appendix

| quantity | equation | relevance |
|---|---|---|
| Debye length | $$\lambda_{D,j}^2 = \frac{\varepsilon_0 k_B T_j}{n_j e^2}$$ $$\lambda_D^2 = \left(\lambda_{D,e}^{-2} + \lambda_{D,i}^{-2}\right)^{-1}$$ | distance around a charge, at which quasi-neutrality is satisfied, $\lambda_D$ is the combined screening length from individual species |
| plasma parameter | $$N_D = n\frac{4}{3}\pi\lambda_D^3$$ | number of particles inside Debye sphere, if $N_D \gg 1$ an ionized gas is considered a plasma (degree of ionization) |
| plasma frequency | $$\omega_{p,j}^2 = \frac{n_j e^2}{\varepsilon_0 m_j} = \frac{v_{th,j}}{\lambda_{D,j}} = \frac{1}{\tau_j}$$ | upper limit for interaction with fields/forces or external excitations inverse screening time |
| thermal velocity | $$v_{th,j}^2 = \frac{k_B T_j}{m_j}$$ | mean velocity from kinetic theory of gases |
| coulomb logarithm | $$\ln(\Lambda)$$ $$\Lambda = \frac{b\max}{b\min} = \lambda_D \cdot \frac{4\pi\varepsilon_0 \mu v_{th}^2}{e^2}$$ | dimensionless scale for transport processes inside discharge fraction of probability for a cumulative 90° scattering by many small pertubation collisions and a single right angle scattering |
| collision frequency | $$\nu_j = \frac{e^4 n_j \ln(\Lambda)}{8\sqrt{2m_j}\pi\varepsilon_0(k_B T_j)^{3/2}}$$ | two body coulomb collision frequency inside species j |
| particle distance & mean free path | $$\bar{b} = \frac{\hbar}{m_j v_{th,j}}$$ $$s_{mfp,j} = \frac{v_{th,j}}{\nu_{j,k}}$$ | mean inter particle distance for species j free flight between subsequent collisions of species j and k with collision frequency $\nu_{j,k}$ |

| quantity | equation | relevance |
|---|---|---|
| speed of sound | $$c_S^2 = \frac{\gamma Z k_B T_e}{m_i}$$ $$\gamma = 1 + 2/f = 5/3$$ | speed of longitudinal ion waves at electron pressure adiabatic coefficient with f, the kinetic degree of freedom |
| Debye-Hückel potential | $$\Phi = \frac{Q}{4\pi\varepsilon|\vec{r}|}e^{-\frac{|\vec{r}|}{\lambda_D}}$$ | electrostatic potential of charge particle $Q$ at distance $|\vec{r}|$, equal to coulomb interaction with additionalshielding by charged particles |
| drift velocity | $$v_{d,j} = u_j = \frac{j_j}{n_j q} = \frac{m\sigma E}{\rho e f}$$ | average velocity of a particle in a conductor with an electric field applied E, where $N$ is the number of free electrons per atom |
| electric mobility | $$\mu_j = \frac{v_d}{E}$$ | ability of charged particle of moving through an electric field — with presence of a conductor |

**Table A.1**: Selection of physical properties of a low temperature ccrf discharge. The index $j$ denotes the species, e.g. electrons, ions. Used quantities can be found in the preface in table 2.

# Bibliography

[1] F. X. Bronold et al. "Radio-frequency discharges in oxygen: I. Particle-based modelling". In: *J. Phys. D: Appl. Phys.* 40 (2007), pp. 6583–6592.

[2] J. Duras. "Instabilities in ion thrusters by plasma-wall interactions". In: *Diplom Thesis* (2011).

[3] V. A. Godyak, R. B. Piejak, and B. M. Alexandrovich. "An experimental system for symmetric capacitive rf discharge studies". In: *Rev. Sci. Instrum.* (1990), pp. 2401–2406.

[4] C. G. Goedde, Allan J. Lichtenberg, and Michael A. Lieberman. "Self-Consistent Stochastic Electron Heating in Radio Frequency Discharges". In: UCB/ERL M88/29 (1988).

[5] G. Gozadinos et al. "Collisionless electron heating by capacitive radio-frequency plasma sheaths". In: *Plasma Sources Sci. Technol.* 10.2 (2001).

[6] E. Kawamura J. T. Gudmundsson and M. A. Lieberman. "A benchmark study of a capacitively coupled oxygen discharge of the oopd1 particle-in-cell Monte Carlo code". In: *Plasma Sources Science and Technology* 22.3 (2013), p. 035011.

[7] D. E. Horne K. Köhler J. W. Coburn and E. Kay. In: *J. Appl. Phys.* 57, 59 (1985).

[8] H. Kawano and F. M. Page. "Experimental methods and techniques for negative-ion production by surface ionization. Part I. Fundamental aspects of surface ionization". In: *International Journal of Mass Spectrometry and Ion Physics* 50.1 (1983), pp. 1 –33. ISSN: 0020-7381.

[9] C. Kullig., J. Meichsner, and K. Dittmann. "Detachment-induced electron production in the early afterglow of pulsed cc-rf oxygen plasmas". In: *Physics of Plasmas* 19 (2012), pp. 73–100.

[10] M. A. Lieberman. "Analytical solution for capacitive RF sheath". In: *IEEE Transactions on Plasma Science* 16.6 (1988), pp. 638–644. ISSN: 0093-3813. DOI: 10.1109/27.16552.

[11] J. Los and J.J.C. Geerlings. "Charge exchange in atom-surface collisions". In: *Physic Reports* 190.3 (1990), pp. 133–190.

[12] P. Matthias. *2D Simulation of RF Discharges.* Ernst-Moritz-Arndt Universität Greifswald, Institute of Physics, 2015.

[13] A. Piel. "Plasma Physics - An Introduction to Laboratory, Space and Fusion Plasmas". In: (2010), pp. 170 ff., 338 ff.

[14] S. Scheuer. "Plasmadiagnostische Untersuchungen zur Charakterisierung von Moden in elektronegativen RF-Plasmen". In: *Master thesis* (2015).

[15] F. J. Schulze. *Electron heating in capacitively coupled radio frequency discharges.* Ruhr-University Bochum, Fakulty of Physics und Astronomy, 2009.

[16] M. Surendra and M. Dalvie. "Moment analysis of rf parallel-plate-discharge simulations using the particle-in-cell with Monte Carlo collisions technique". In: *Phys. Rev. E* 48 (5 1993), pp. 3914–3924. DOI: 10.1103/PhysRevE.48.3914.

[17]   D. Tskhakaya et al. "The Particle-In-Cell Method". In: *Contrib. Plasma Phys.* 47.8-9
       (2007), pp. 563–594.

[18]   S. Ustaze et al. "Electron Capture and Loss processes in the Interaction of Hydrogen,
       Oxygen and Fluorine Atoms and Negative Ions with a MgO(100) Surface". In: *Physical
       Review Letters* 79.18 (1997), pp. 3526–3529.